Biosensors and Bioelectronics 123 (2019) 51–58

Contents lists available at ScienceDirect

Biosensors and Bioelectronics

journal homepage: www.elsevier.com/locate/bios

Two-dimensional oriented growth of Zn-MOF-on-Zr-MOF architecture: A highly sensitive and selective platform for detecting cancer markers

Nan Zhou[a], Fangfang Su[b], Chuanpan Guo[b], Linghao He[b], Zhankui Jia[a,*], Minghua Wang[b], Qiaojuan Jia[b], Zhihong Zhang[b,*], Siyu Lu[c,*]

[a] The First Affiliated Hospital of Zhengzhou University, Zhengzhou, China
[b] Henan Provincial Key Laboratory of Surface and Interface Science, Zhengzhou University of Light Industry, No. 136, Science Avenue, Zhengzhou 450001, China
[c] College of Chemistry and Molecular Engineering, Zhengzhou University, Zhengzhou 450000, China

ARTICLE INFO

Keywords:
Bimetallic ZnZr-metal organic frameworks
Electrochemical aptasensor
Detection of protein tyrosine kinase-7
MOF-on-MOF hybrids

ABSTRACT

Fabricating novel bimetallic metal organic framework (MOF) architectures and exploiting them as aptasensor scaffolds for detecting diverse analytes, especially cancer markers, have aroused widespread research attention. Herein, we report a novel strategy for obtaining ZnZr bimetallic MOFs via the MOF-on-MOF method and exploit them as an aptasensor platform for detecting the cancer marker protein tyrosine kinase-7 (PTK7). Basic characterizations reveal that the chemical structure, crystalline properties, and surface functionality of bimetallic ZnZr-MOFs can be modulated by changing the order of addition of metal precursors and organic ligands. The Zn-MOF-on-Zr-MOF hybrid exhibits a hierarchically decussated foliace, whereas Zr-MOF-on-Zn-MOF demonstrates a multilayered nanosheet structure. The electrochemical results reveal that Zr-MOF facilitates aptamer strand immobilization, whereas the Zn-MOF stabilizes the G-quadruplex formed by aptamer strands and PTK7. The Zn-MOF-on-Zr-MOF-based aptasensor outperforms the Zr-MOF-on-Zn-MOF-based one, providing ultralow detection limits of 0.84 and 0.66 pg mL^{-1}, as obtained by electrochemical impedance spectroscopy and differential pulse voltammetry, respectively, within the PTK7 concentration range of 1.0 pg mL^{-1} to 1.0 ng mL^{-1}. The proposed Zn-MOF-on-Zr-MOF-based aptasensor exhibits high selectivity in the presence of various interferences, good stability, reproducibility, and acceptability in human serum. The proposed strategy provides a new approach for fabricating ultrasensitive and selective bimetallic MOFs-based aptasensors and contributes to efforts to broaden their applications in early cancer diagnosis.

1. Introduction

As an important biomarker for a range of leukemias and solid tumors, the cell membrane protein tyrosine kinase-7 (PTK7) was first identified in melanocytes and subsequently found to play a role in regulating neural development and planar cell polarity in vertebrates, as well as morphogenetic cell movement, during embryonic development (Shangguan et al., 2008). Given that the exact functions of PTK7 in different tumors remain unclear, effective detection of PTK7 is pivotal to understand the dynamic roles of this membrane protein in cells and clinical diagnosis. Aptamers, which are oligonucleotides (ssDNA or RNA) with a three-dimensional (3D) structure characterized by loops or hairpins, are widely used for variable target detection (e.g., cancer cells, protein, heavy metal ions, adenosine triphosphate) (Ma et al., 2015). Compared with monoclonal antibodies, aptamers possess low molecular weights and can be chemically synthesized and readily modified; as such, these molecules present many favorable features, including high binding affinity, specificity, and controllable structures (Zhang et al., 2015).

Z. Liu et al. (2017) employed a protein-triggered DNA release and AgNC transfer-based strategy to achieve the rapid, facile, and sensitive detection of PTK7. A novel aptasensor based on (+)AuNPs/NF/GCE showed a low detection limit of 372 fM when detecting PTK7 (Miao et al., 2016). Many efforts have been exerted to develop detection methods for PTK7. However, conventional techniques, such as enzyme-linked immunosorbent assay (Zhou et al., 2011), mass spectrometry (Jung et al., 2015), and fluorescence correlation spectroscopy (Chen et al., 2009), usually require tedious pretreatment (separation, purification, and concentration), thereby rendering them inappropriate for in situ detection. In comparison with other methods, electrochemical approaches are known to be simpler and more efficient tools due to their low-cost instrumentation, fast operation, and excellent

* Corresponding authors.
E-mail addresses: jiazhankui@126.com (Z. Jia), 2006015@zzuli.edu.cn (Z. Zhang), sylu2013@zzu.edu.com (S. Lu).

https://doi.org/10.1016/j.bios.2018.09.079
Received 17 July 2018; Received in revised form 3 September 2018; Accepted 21 September 2018
Available online 22 September 2018
0956-5663/

performance. As such, detection methods based on this approach have drawn considerable research attention in recent years (Jia et al., 2016). The detection sensitivity and efficiency of electrochemical assays mainly depend on the features of the electrode material, such as its electrochemical activity, particle homogeneity, binding affinity with the electrode, and biocompatibility (Q. Wang et al., 2017; S. Wang et al., 2017). Therefore, the development of novel nanomaterials to fabricate extremely sensitive and selective aptasensors to detect PTK7 is highly desired.

Metal−organic frameworks (MOFs), which consist of multidentate organic building blocks and metal or metal-cluster secondary building units, have rapidly emerged as new porous materials with potential use in various fields (Zhu and Xu, 2014). MOFs have been evaluated for their applicability as a suitable platform for biosensing owing to their various grafting groups (e.g., $-NH_2$ or $-COOH$) (Hou et al., 2017), $\pi-\pi$ stacking, hydrogen bonding, and electrostatic interactions with negatively charged nucleic acid sequences (Xie et al., 2018). A series of new biosensors based on MOFs have been fabricated to detect cancer markers (Huang et al., 2017), antibiotics, heavy metal ions (Zhao et al., 2016), and other analytes (Ren et al., 2017). Zr-based MOFs possess excellent stability and high affinity toward the phosphate groups of biomolecules (C. Liu et al., 2017; Zhang et al., 2017; Zhao et al., 2014). DNA strands can be immobilized onto Zn-based MOFs to fabricate biosensors (Sun et al., 2017). Zn-MOFs show high affinity toward ssDNA and dsDNA and highly selective and sensitive detection ability for nitroaromatic explosives (Wang et al., 2014). To date, however, no Zn-MOF- or bimetallic ZrZn-MOF-based electrochemical aptasensor has yet been reported. Thus, development of ZnZr-MOF-based aptasensors for determining cancer markers via the electrochemical technique is a worthwhile endeavor.

Conventional MOFs are composed of agglomerated powders with micrometer-sized crystals or barely dispersible nanoparticles and present a 3D structure (Quah et al., 2016). The difficulty of uniformly dispersing MOF particles in aqueous solutions on account of their large size leads to their instability and tendency to fall off when coated onto the surface of the substrate; conventional MOFs, therefore, have limited applications in biosensing. To address this issue, 2D MOF nanosheets were recently developed; these nanosheets present unique properties, good dispersibility, and large surface areas for adequate protein binding (Jung et al., 2011). 2D Zr-MOF and Zn-MOF nanosheets have been used as biosensor sensitive layers (He et al., 2017; Tan et al., 2017). Despite their obvious benefits, however, 2D MOFs-based aptasensors fabricated from a single MOF precursor suffer several limitations, including poor conductivity, low activity, and distorted shapes, all of which are unfavorable for electrochemical detection (Shen et al., 2015).

Different types of MOFs can be combined to form hybrid MOFs containing more than two types of MOFs into one particle, and methods to do so are a central goal in MOF development. Bimetallic MOFs often display enhanced framework hydrostability compared with single-parent MOFs (Song et al., 2013). In light of their excellent compatibility with different metal species, bi-/multi-metallic MOFs can be successfully obtained via a post-synthesis method (Qian et al., 2017), transmetalation (Bellarosa et al., 2015), and a ligand-oriented bifunctional method (Qian et al., 2016). The use a previously synthesized MOF to grow another MOF on the surface of the MOF matrix by lattice matching is an alternative that allows the formation of core–shell MOF-on-MOF hybrids via the epitaxial growth method (Gu et al., 2017). The MOF-on-MOF method is a potential approach with which to form 2D hybrid MOFs. To the best of our knowledge, the application of bimetallic MOF nanosheets as novel platforms for sensitive detection of PTK7 has not been reported.

In the present work, we synthesize two novel types of bimetallic ZnZr-based MOFs for the first time via the MOF-on-MOF method and employ these MOFs as scaffold substrates for aptasensors to achieve sensitive PTK7 detection (Scheme 1). The bimetallic ZnZr-MOFs were prepared by altering the order of addition of the metal ion precursors and ligands to obtain Zn-MOF-on-Zr-MOF and Zr-MOF-on-Zn-MOF. The Zn-MOF-on-Zr-MOF-based aptasensor clearly outperforms the Zr-MOF-on-Zn-MOF-, Zn-MOF-, and Zr-based sensors. Compared with other routine PTK7 aptasensors, the Zn-MOF-on-Zr-MOF-based aptasensor not only provides stronger bioaffinity toward aptamer strands (because of Zr-MOF) but also possesses higher stabilizing ability for the G-quadruplex complex formed between the aptamer strands and PTK7 (because of Zn-MOF). Overall, the Zn-MOF-on-Zr-MOF-based aptasensor exhibits high selectivity, good stability and reproducibility, and acceptable applicability.

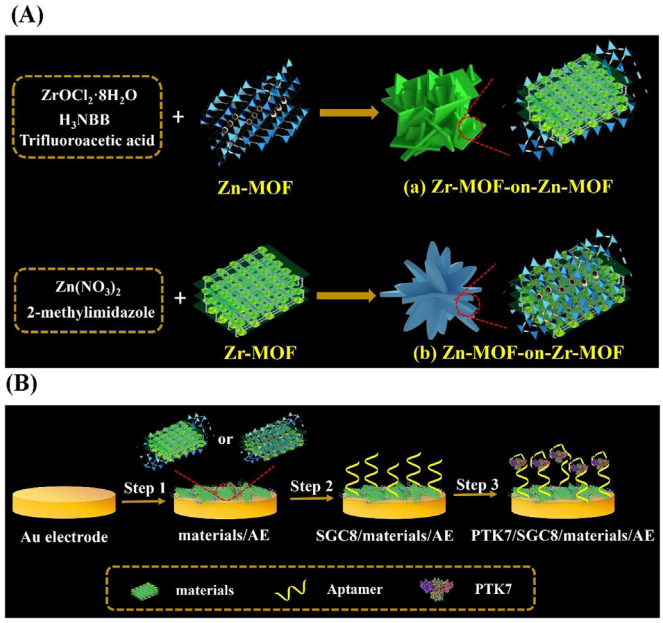

Scheme 1. (A) The schematic diagram of the synthesis procedures for two kinds of ZnZr-MOFs, including (a) Zn-MOF-on-Zr–MOF and (b) Zr-MOF-on-Zn-MOF hybrids and (B) the detection procedure toward PTK7, including the AE modified with Zn-MOF-on-Zr–MOF or Zr-MOF-on-Zn-MOF hybrid (Step 1), the SGC8 aptamer immobilization over the modified AE (Step 2), and the PTK7 detection (Step 3).

2. Experimental section

The part of material and regents, preparation of solutions, and basic characterizations are supplied in the Supporting Information (S1).

2.1. Preparation of Zn-MOF-on-Zr–MOF and Zr-MOF-on-Zn-MOF hybrids

The 2D Zn-MOF nanosheets were synthesized according to the reported literature (Fang et al., 2017). In brief, $Zn(NO_3)_2$ (0.595 g, 2.0 mmol) was dissolved ultrasonically in Milli-Q water (20 mL) to prepare Solution A. 2-Methylimidazole (1.3 g) was dissolved in Milli-Q water (20 mL) to prepare Solution B. Then Solution A was quickly added into Solution B. The mixture was placed at room temperature for 4 h before centrifugation. Finally, the precipitate was washed three times with Milli-Q water and dried at 60 °C to obtain the 2D Zn-MOF powder.

The 2D Zr-MOF nanosheets were synthesized according to the previous work (Zhang et al., 2017). Typically, $ZrOCl_2·8H_2O$ (175.0 mg, 0.5 mmol) was dissolved ultrasonically in a mixture of DEF (3 mL) and trifluoroacetic acid (0.5 mL) in a 10 mL screw-capped vial for 10 min. Then, H_3NBB (80.0 mg, 0.1 mmol) was dissolved ultrasonically in DEF (3 mL) for 10 min. Finally, the homogeneous mixture was stirred for 2 days under 50 °C. The resulting yellow suspension was isolated by centrifugation at 10,000 rpm for 3 min and then washed for three times with DMF to remove the unreacted precursor and collected by

centrifuging at 10,000 rpm for 3 min. As a result, pure Zr-MOF powder was obtained.

In order to obtain the Zn-MOF-on-Zr-MOF structure, the as-prepared 2D Zr-MOF nanosheets (100 mg) were added into the preparation system of the 2D Zn-MOF nanosheets (Scheme 1A). Additionally, the as-obtained Zn-MOF nanosheets (30 mg) were added into the procedure of the 2D Zr-MOF to prepare the Zr-MOF-on-Zn-MOF hybrid (Scheme 1A).

2.2. Pre-treatment of the bare Au electrode

Bare Au electrode (AE) with 3 mm diameter was obtained from Gaoss Union instrucment Inc. (Wuhan, China) and cleaned prior to use. Firstly, the AE was polished with 0.05 μm alumina slurry and rinsed with Milli-Q water. Afterward, the AE was cleaned in piranha solution (v/v, H_2SO_4:H_2O_2 = 7:3) for 15 min, following washed with Milli-Q water, and dried under nitrogen. Finally, the AE was electrochemically activated in 0.5 M H_2SO_4 by potential cycling between − 0.2 V and 1.6 V, then rinsed with Milli-Q water and dried under nitrogen.

2.3. Fabrication of the electrochemical aptasensors

In the present work, four kinds of aptasensors based on Zn-MOF, Zr-MOF, Zn-MOF-on-Zr–MOF, and Zr-MOF-on-Zn-MOF were developed. The resultant nanomaterial powder of 0.1, 0.5, 1.0, 2.0, and 5.0 mg mL^{-1} was dispersed in 1.0 mL of deionized water, followed by ultrasonically agitating for 30 min to form a homogeneous suspension liquid with different concentrations of 0.1, 0.5, 1.0, 2.0, and 5.0 mg mL^{-1}. Taking the Zn-MOF-on-Zr–MOF-based aptasensor as example, the aptasensor for detecting PTK7 was fabricated as the following steps (Scheme 1B). Firstly, 5.0 μL of Zn-MOF-on-Zr-MOF aqueous suspension (1.0 mg mL^{-1}) was dropped onto the pre-treated AE surface, following by drying with ultrapure N_2 (**Step 1**). Subsequently, the Zn-MOF-on-Zr-MOF-modified AE was immersed in 0.1 M PBS (pH = 7.4) to remove the weakly bound nanomaterial (denoted as Zn-MOF-on-Zr-MOF/AE). Afterward, the Zn-MOF-on-Zr-MOF/AE was incubated with the PTK7 aptamer solution to anchor the aptamer strands (denoted as Apt/Zn-MOF-on-Zr-MOF/AE), following by sufficiently rinsing with PBS to remove the weakly adsorbed aptamer strands and dried over a gentle stream of N_2 (**Step 2**). Thus, the developed Apt/Zn-MOF-on-Zr-MOF/AE aptasensor was obtained and used to detect PTK7 for further electrochemical measurements (**Step 3**).

Similarly, for comparison, various aptasensors based on Zn-MOF, Zr-MOF, and Zr-MOF-on-Zn-MOF were also developed in the same way with the Zn-MOF-on-Zr-MOF-based one. Additionally, all aptasensors were stored at 4 °C in a refrigerator when not in use.

2.4. Electrochemical measurements

Electrochemical impedance spectroscopy (EIS), cyclic voltammetry (CV), and differential pulse voltammetry (DPV) were performed on a CHI 660E electrochemical station (Shanghai Chenhua, China) with a three-electrode system. The system includes the AE, Ag/AgCl electrode, and Pt wire, which were used as the working, reference, and counter electrodes, respectively. The measurements were conducted in 0.1 M PBS (pH = 7.4) containing 5.0 mM $K_3[Fe(CN)_6]/K_4[Fe(CN)_6]$ (1:1). CV curves were recorded within –0.2–0.8 V vs Ag/AgCl with a scan rate of 100 mV s^{-1}. EIS measurements were performed in the frequency range of 0.01–100 kHz with a direct current potential of 0.22 V as a bias potential and the amplitude was 5.0 mV. The response value was analyzed by Zview2 software. DPV was collected within − 0.2–0.8 V, with amplitude 50 mV, pulse width 0.2 s, and sampling width 0.0167 s. As for the evaluation of the limitation of detection toward PTK7, the Apt/Zn-MOF-on-Zr-MOF/AE was immersed in the PTK7 solution with different concentrations (denoted as PTK7/Apt/Zn-MOF-on-Zr-MOF/AE) for 30 min and measured by EIS. After each detection step, the electrode was rinsed with PBS thoroughly to remove the weakly bound molecules. Notably, five parallel experiments were performed each time, and the average values were used in the present work.

3. Results and discussion

3.1. Design for the PTK7 aptasensor

We synthesized two types of bimetallic ZnZr-MOFs by changing the order of addition of Zn-MOF and Zr-MOF to the reaction system and obtained Zn-MOF-on-Zr-MOF and Zr-MOF-on-Zn-MOF. These materials were then exploited as the scaffold materials of aptamer sensors to detect PTK7. The organic linkers in MOFs usually possess unique functional groups and offer a source of π−π stacking, hydrogen bonding, and electrostatic interactions with negatively charged nucleic acid sequences (Sun et al., 2017). Zr-MOF shows excellent stability, low toxicity, and high affinity toward the phosphate groups of DNA or RNA; thus, Zr-MOF-based biosensors could be developed to detect various analytes (Guo et al., 2017; Q. Wang et al., 2017; S. Wang et al., 2017; Zhang et al., 2017). After the aptamer strands are immobilized onto the MOF-on-MOF substrates, specific binding of PTK7 with the SGC8 aptamer triggers a structural change in the aptamer (Lin et al., 2015). Conformational changes in the aptamer strands can lead to changes in electrochemical signals, which are then determined by electrochemical techniques (Miao et al., 2016). Different MOF-on-MOF architectures result in various surface and electrochemical performances, further altering the sensing efficiency of the aptamers.

3.2. Chemical structure and component of Zn-MOF-on-Zr-MOF

The XRD patterns and FT-IR and XPS spectra of Zn-MOF, Zr-MOF, Zr-MOF-on-Zn-MOF, and Zn-MOF-on-Zr-MOF were employed to characterize the crystalline and chemical structures of the materials. As discussed in **S2** (Supporting Information), the chemical and crystalline features of the bimetallic MOF-on-MOF composites mainly depend on the outer layer (Fig. S1). The XPS survey spectra of all samples are illustrated in Fig. S2, and the atomic% content of each element contained in all samples is summarized in Table S1. To evaluate the chemical valence and environment of each element in the as-developed nanocomposites, we deconvoluted the high-resolution XPS spectra these elements using XPSPEAK1 software, and display the core-level XPS spectra of each element containing Zn-MOF and Zr-MOF in Figs. S3 and S4. The Zn 2*p* and Zr 3*d* core-level XPS spectra of Zn-MOF-on-Zr-MOF and Zr-MOF-on-Zn-MOF are shown in Fig. 1, and their C 1*s*, N 1*s*, and O 1*s* core-level XPS spectra are illustrated in Fig. S5. The bimetallic Zn-MOF-on-Zr-MOF hybrid exhibits the clear coexistence of Zn 2*p* and Zr 3*d* signals, the core-level spectra of which are similar to those of Zn-

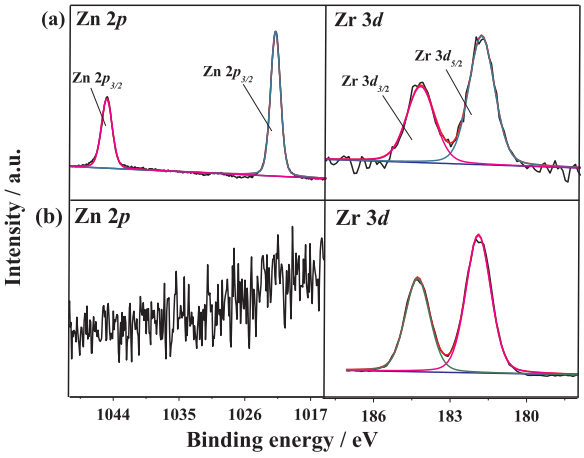

Fig. 1. Zn 2*p* and Zr 3*d* core-level XPS spectra of (a) Zn-MOF-on-Zr-MOF and (b) Zr-MOF-on-Zn-MOF hybrids.

MOF and Zr-MOF, respectively. No clear Zn 2*p* signal of the Zr-MOF-on-Zn-MOF hybrid is observed. The chemical structure of the interior layers of the materials cannot be determined due to the thickness limitation of XPS (Cumpson, 2000). The Zr 3*d* deconvolution peaks are also similar to those of Zr-MOF, indicating that the surface performance of the Zr-MOF-on-Zn-MOF hybrid is close to that of the pristine Zr-MOF. The C 1 *s*, N 1 *s*, and O 1 *s* core-level XPS spectra of these two samples confirm this conclusion (Fig. S5). The presence of Zn 2*d* peaks suggests that the Zr-MOF substrate promotes the penetration of Zn(II) ions into the Zr-MOF nodes, leading to complete integration of Zn-MOF and Zr-MOF (He et al., 2017). By contrast, Zr(IV) ions cannot easily penetrate the Zn-MOF interior because of the small pore size of the latter; thus, Zr-MOF covers the Zn-MOF surface (Chen et al., 2013). Various growth mechanisms of the Zr-MOF-on-Zn-MOF and Zn-MOF-on-Zr-MOF hybrids lead to different DNA adsorption behaviors and, in turn, different sensing behaviors toward analytes.

3.3. Surface morphology of Zn-MOF-on-Zr-MOF and Zr-MOF-on-Zn-MOF

FE-SEM images of pristine Zn-MOF and Zr-MOF are illustrated in Fig. S6. Zn-MOF exhibits typical leaf-like nanosheets (Figs. S6a and S6b) (Fang et al., 2017). As displayed in Figs. S6c and S6d, the synthesized Zr-MOF is composed of a large number of agglomerated sheets with a width of several micrometers (He et al., 2017). Zn-MOF-on-Zr-MOF clearly exhibits a unique flower-like structure with a size of approximately 10 ± 2 μm (Fig. 2a and b). The TEM image of the Zn-MOF-on-Zr-MOF hybrid (Fig. 3a) shows decussated nanosheets but no clear lattice spacing (Fig. 3b). As shown in Fig. 2**c** and **d**, the surface morphology of the Zr-MOF-on-Zn-MOF hybrid is similar to that of pristine Zr-MOF. The TEM image of Zr-MOF-on-Zn-MOF shows identical lattice fringes widely distributed in the locations marked in Fig. 3**c** and **d**. A clear spacing of 2.03 nm, corresponding to the (220) reflection of ZrO_2 (Chuah et al., 1996), is also observed. These results reveal that the external layers of the Zn-MOF-on-Zr-MOF and Zr-MOF-on-Zn-MOF hybrids are completely different, in agreement with their XPS characterizations.

3.4. Electrochemical sensing performances of all samples

Bimetallic Zn-MOF-on-Zr-MOF, Zr-MOF-on-Zn-MOF, Zn-MOF, and Zr-MOF were employed to fabricate aptasensors for detecting PTK7. To evaluate the electrochemical characteristics of the developed aptasensors, $[Fe(CN)_6]^{3-/4-}$ was used as the probe in the electrochemical impedance spectroscopic (EIS) measurements. As displayed in Figs. S7 and Fig. 4a, the EIS Nyquist plots of the whole procedure of the PTK7 detection using the Zn-MOF-, Zr-MOF-, Zr-MOF-on-Zn-MOF-, and Zn-MOF-on-Zr-MOF-based aptasensors are summarized and analyzed using the fitted circuit (Inset of Fig. 4a). It is clear that the circuit is composed of four elements, including the solution resistance (R_s), the constant phase element (CPE), a Warburg impedance (W), and the charge transfer-resistance (R_{ct}) (Narayanan et al., 2015). Among them, the Warburg impedance represents the impedance of diffusion electroactive species from bulk solution to the interfacial region and usually appears as a straight line with a slope of 45° (Tertiş et al., 2015). The semicircle diameter equals to R_{ct}, revealing the blocking behavior of the electrode surface for the redox couple. In consequence, it can be used as a signal to characterize the modification for each step. The values obtained for the elements R_s, R_{ct}, CPE, α, and W for the bare AE and different steps for the aptasensor fabrication using Zr-MOF-on-Zn-MOF- or Zn-MOF-on-Zr-MOF hybrid are shown in Table S2. As shown in Table S3**,** the fitting values of Warburg impedance did not exhibit a linear dependence on PTK7 concentration, and were not used for analytical purposes. The difference of R_{ct} (ΔR_{ct}) can be represented as the following equation:

$$\Delta R_{ct} = R_{ct,i+1} - R_{ct,i} \quad (1)$$

where $R_{ct,\ i+1}$ and $R_{ct,\ i}$ are the electron transfer resistance before and after each step, including the AE modified with variously prepared materials ($\Delta R_{ct} = R_{ct,\ materials} - R_{ct,\ AE}$), the aptamer immobilization ($\Delta R_{ct} = R_{ct,\ aptamer\ \text{immobilization}} - R_{ct,\ materials}$), and the PTK7 detection

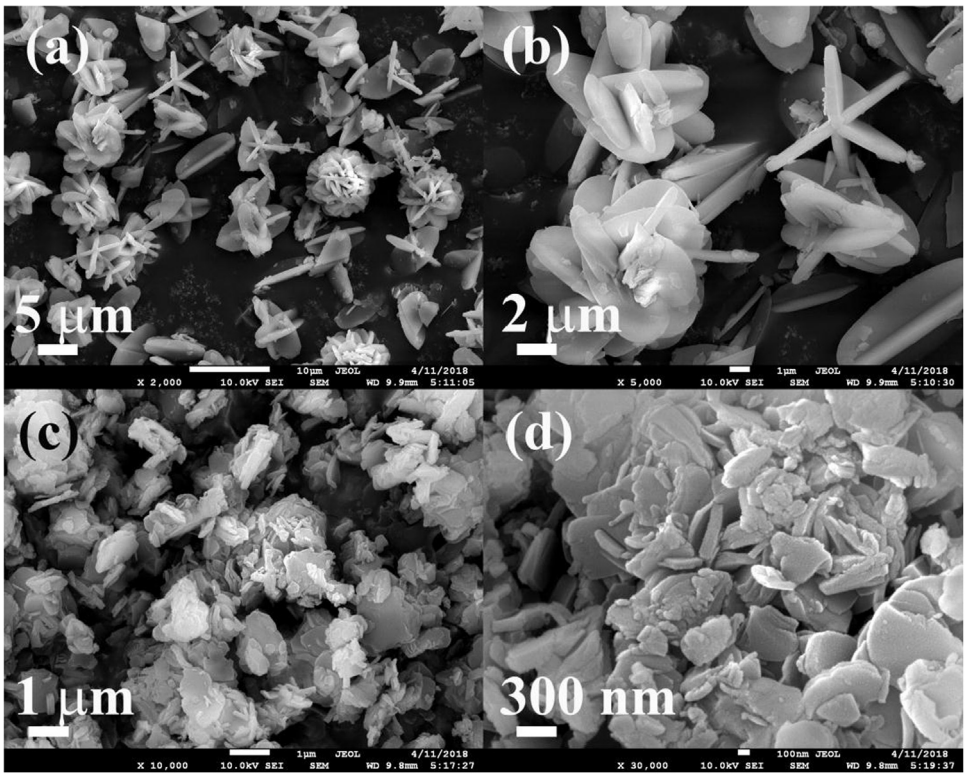

Fig. 2. Low- and high-magnification SEM images of (a, b) Zn-MOF-on-Zr-MOF and (c, d) Zr-MOF-on-Zn-MOF hybrids.

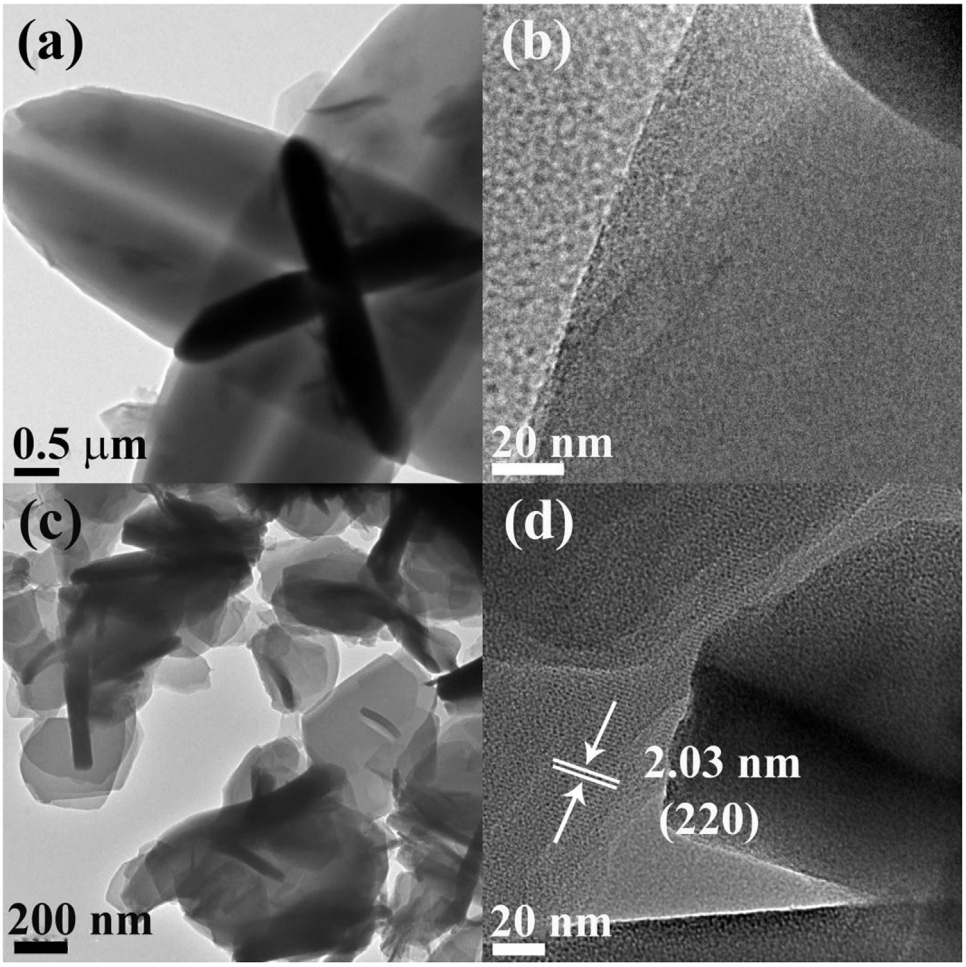

Fig. 3. TEM and HR-TEM images of (a, b) Zn-MOF-on-Zr-MOF and (c, d) Zr-MOF-on-Zn-MOF hybrids.

(ΔR_{ct} = $R_{ct,\ PTK7\ detection}$ − $R_{ct,\ aptamer\ immobilization}$). Thus, ΔR_{ct} can be utilized for the quantitative the overlayer adhered to the electrode (Gao et al., 2015).

Fig. 4a illustrates the Nyquist plots of Zn-MOF-on-Zr-MOF-based aptasensor during PTK7 detection. All of the plots show nearly straight lines, which is a characteristic of a diffusion-limiting process. As expected, the bare AE shows a small R_{ct} of 54.1 Ω, which indicates its good electrochemical activity. After modification with the Zn-MOF-on-Zr-MOF, the R_{ct} of the electrode increases to 162.1 Ω. This result is mainly attributed to the blocking effect brought about by the poor electrochemical performance of the bimetallic MOF (Wang et al., 2009). As the aptamer strands onto the Zn-MOF-on-Zr-MOF-modified AE, R_{ct} successively increases to 287.8 Ω. Aptamer strands can be ionized into negatively-charged particles, thereby limiting the access of negatively charged $[Fe(CN)_6]^{3-}/^{4-}$ redox ions to the electrode surface (Salamon et al., 2015) and increasing R_{ct}. In the presence of PTK7, the diameter of the Nyquist plot reaches 451.7 Ω. The G-quadruplex structure formed compels conformational changes in the aptamer strands due to their recognition of PTK7, which prevents redox ions from transferring to the electrode surface (Lin et al., 2015). The Nyquist plots of the Zn-MOF-, Zr-MOF-, and Zr-MOF-on-Zn-MOF-based aptasensors during PTK7 detection are displayed in Fig. S7. The standard deviations of each R_{ct} are summarized in Table S4. The R_{ct} obtained at each step of the detection procedure increase in the order of electrode modification, anchoring of aptamer strands, and PTK7 detection. Different ΔR_{ct} values at each step are obtained from the different sensing systems, thereby reflecting differences in the amounts of aptamer strands adsorbed and sensing performance. We calculated the ΔR_{ct} for the four sensing systems developed in this work and illustrate the results in Fig. 4b. Schematics of the possible mechanisms of action of the Zr-MOF-on-Zn-MOF- and Zn-MOF-on-Zr–MOF hybrid-based aptasensors for detecting PTK7 are illustrated in Scheme 2. In the Zr-MOF-on-Zn-MOF-based aptasensor, electrode modification caused a large ΔR_{ct} of 160.5 Ω owing to the relatively poor electrochemical activity of the Zr-MOF-on-Zn-MOF hybrid. After anchoring of the aptamer strands, the ΔR_{ct} of the sensor increased to 112.3 Ω, indicating a large amount of aptamer adsorption. After PTK7 detection, the $\triangle R_{ct}$ decreased to only 50.8 Ω. This result shows that the sensing behavior of the Zr-MOF substrate toward PTK7 is similar to that of our reported 493-MOF-NA sensor (C. Liu et al., 2017). The strong interaction between phosphate groups in the aptamer strands and Zr(IV) of Zr-MOF via the chemical bond Zr–O–P (Asha et al., 2016) can take place in the strands, it can result in that most of long aptamer strand with 39 mer bases lie over the framework surface (**Step (I)**). Therefore, the aptamer strands cannot easily undergo conformational changes, and PTK7 cannot bind with these strands (**Step (II)**).

This result can also be explained by the large specific surface area of the Zr-MOF-on-Zn-MOF hybrid. As displayed in Fig. S8, the N_2 adsorption–desorption isotherms of the two hybrids are measured. The specific surface areas of Zr-MOF-on-Zn-MOF and Zn-MOF-on-Zr-MOF are 23.8 and 6.01 $m^2\ g^{-1}$, respectively. The large specific area of the Zr-MOF-on-Zn-MOF hybrid can provide additional active sites for anchoring large amounts of aptamers and signal probes, leading to high signal outputs (Yu et al., 2018; Wu et al., 2017). Although the ΔR_{ct} of the Zn-MOF-on-Zr–MOF-based aptasensor obtained for aptamer immobilization is comparable with that of the Zr-MOF-on-Zn-MOF-based

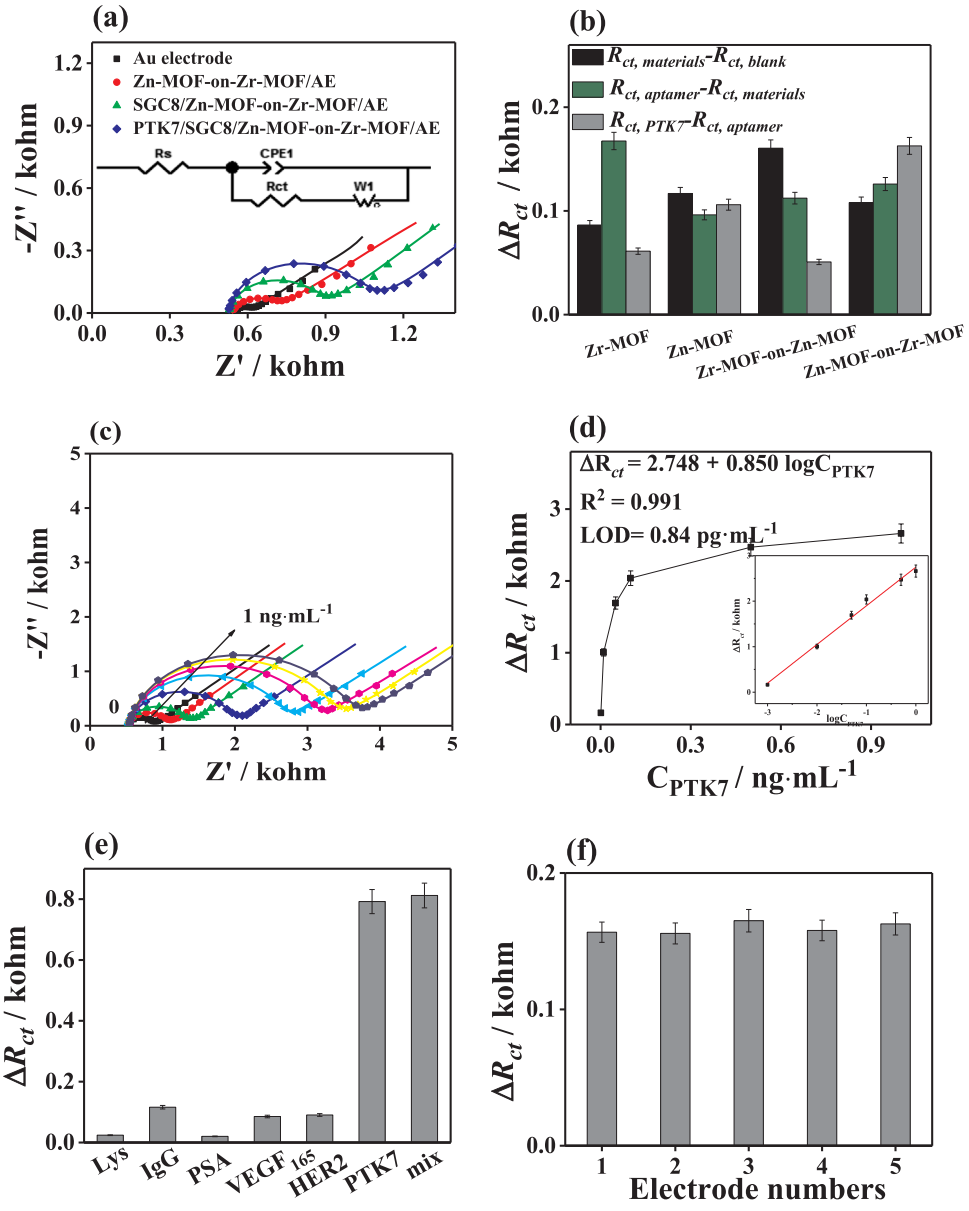

Fig. 4. (a) EIS Nyquist plots of Zn-MOF-on-Zr-MOF-modified Au electrode for the detection of 0.001 ng mL^{-1} PTK7. (b) Variation in the charge-transfer resistance (R_{ct}) values for each stage in the detection of PTK7. (c) EIS responses of the Zn-MOF-on-Zr-MOF/AE with different PTK7 concentrations (0, 0.001, 0.005, 0.01, 0.05, 0.1, 0.5, and 1 ng mL^{-1}). (d) Dependence of ΔR_{ct} on the concentration of PTK7 (Inset: the linear parts of the calibration curves). (e) ΔR_{ct} values of Zn-MOF-on-Zr-MOF-based electrochemical aptasensor by separately adding the interferences (Lys, IgG, PSA, $VEGF_{165}$ and HER2 with the concentration of 0.05 ng mL^{-1}), PTK7 (0.001 ng mL^{-1}), and their mixture. (f) Reproducibility of the Zn-MOF-on-Zr-MOF-based aptasensor for detecting PTK7 with the concentration of 0.001 ng mL^{-1}.

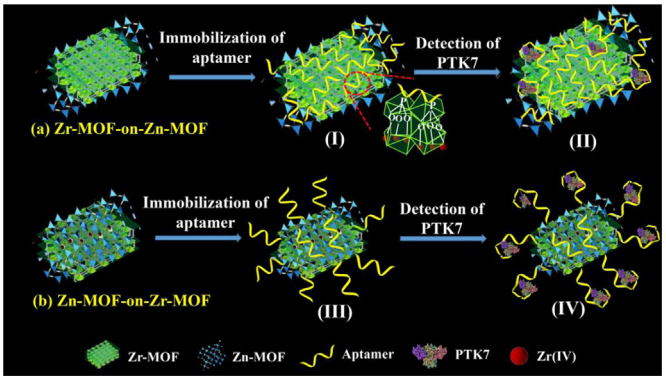

Scheme 2. The mechanism diagram of the aptasensors based on Zn-MOF-on-Zr–MOF and Zr-MOF-on-Zn-MOF hybrids.

aptasensor (125.9 Ω), the observed ΔR_{ct} for detecting PTK7 is large (162.7 Ω). The aptamer strands can be immobilized over the Zn-MOF-on-Zr-MOF substrate via binding forces brought about by N atoms in the imidazole rings of dimethyl imidazole (Dash et al., 2011); other high-binding interactions, such as π−π stacking, electrostatic interactions between positively charged nitrogen-related groups, and the negatively charged phosphate groups of aptamer strands (He et al., 2014), may also occur. The combined effects of these interactions allow the aptamer strands to anchor onto the Zn-MOF surface, leaving one end free (**Step (III)**). This mechanism improves the conformational changing ability of the aptamer strands to recognize PTK7 and form the G-quadruplex complex (**Step (IV)**).

Similar observations are obtained for the Zr-MOF- and Zn-MOF-based aptasensors. These sensors exhibit very strong immobilization of the aptamer strands, although their PTK7 detection effects show substantial differences. The ΔR_{ct} values of the Zn-MOF-based aptasensor and Zr-MOF sensing system after PTK7 binding are 106 and 61.2 Ω, respectively. This result demonstrates that the surface performance of the electrode materials plays an important role in analyte detection. The detection sensitivity of the same bimetallic-based MOFs for analytes in aqueous solution can be modulated by changing the formation mechanism of the hybrids.

The Zn-MOF-on-Zr-MOF hybrid was selected as the scaffold material for aptasensor fabrication to further assess its sensing performance for detecting PTK7. To probe the effect of Zn-MOF-on-Zr-MOF coverage on

PTK7 detection, we constructed four of aptasensors with 0.1, 0.5, 2.0, and 5.0 mg mL^{-1} Zn-MOF-on-Zr-MOF and then determined PTK7 under the same conditions by EIS (Fig. S9). The R_{ct} obtained after PTK7 detection increased with increasing dosage of the Zn-MOF-on-Zr–MOF hybrid from 0.1 mg mL^{-1} to 1.0 mg mL^{-1}. When the usage of the Zn-MOF-on-Zr–MOF hybrid exceeded 1.0 mg mL^{-1}, adherence to the AE surface was difficult. This result could be mainly attributed to the excessive thickness of the sensing layer. The fabricated electrode was unstable in aqueous solutions and showed false determination results. Therefore, 1.0 mg mL^{-1} Zn-MOF-on-Zr-MOF was employed to fabricate the aptasensor in subsequent experiments.

We performed CV and DPV on the Zn-MOF-on-Zr-MOF-modified electrode at different steps, and PTK7 detection was carried out using 5.0 mM $K_3[Fe(CN)_6]/K_4[Fe(CN)_6]$ (1:1) mixture as a redox probe, as displayed in Fig. S10. The peak current of all CV curves continuously decreased along with the order to construct aptasensor, including the modification of AE with the Zn-MOF-on-Zr-MOF, the aptamer immobilization, and the detection of PTK7 (Fig. S10a). This result indicates that each process on the AE surface restricts the access of electrons to the transistor surface, leading to a low efficiency of electron transfer. The same results are observed in the DPV measurements; here, the peak current (I_p) successively decreased in the order of modification of the Zn-MOF-on-Zr-MOF electrode, aptamer immobilization, and PTK7 detection (Fig. S10b). These findings are consistent with the previous EIS results.

3.5. Sensitivity of the developed Zn-MOF-on-Zr-MOF-based aptasensor

To evaluate the analytical performance of the developed aptasensor, we incubated Zn-MOF-on-Zr-MOF/AE with different concentrations of PTK7 and subsequently measured them by EIS, as shown in Fig. 4c. The diameters of the Nyquist plots of the Zn-MOF-on-Zr-MOF-based sensor increased with increasing PTK7 concentration because more PTK7 molecules can combine with the aptamer strands at higher analyte concentrations (Yıldız, 2015), leading to strong blocking of electron transfer toward the electrode surface and improvements in R_{ct}. When the ΔR_{ct} ($R_{ct,\ PTK7} - R_{ct,\ material}$) of the developed aptasensor before and after PTK7 detection is referred to as the determined signal (Fig. 4d), ΔR_{ct} is highly proportional to the logarithm of the PTK7 concentration (log C_{PTK7}). The linear regression equation is ΔR_{ct} (ohm) = 2748 + 850 log C_{PTK7} (ng mL^{-1}), with a correlation coefficient (R^2) of 0.991. According to the Langmuir adsorption equation (Schmitt et al., 2007), the limit of detection (LOD) was calculated to be 0.84 pg mL^{-1} at a signal-to-noise (S/N) ratio of 3 within the PTK7 concentration range of 0.001–1.0 ng mL^{-1}.

The DPV technique was used to investigate the analytical performance of the developed Zn-MOF-on-Zr-MOF-based aptasensor (Fig. S11). PTK7 solutions of various concentrations were incubated with the electrochemical measurement system, and the Ip of the electrode was observed to decrease with increasing PTK7 concentration (Fig. S11a). Taking ΔI_p ($\Delta I_p = I_{p,\ PTK7} - I_{p,\ material}$) as the determined signal (Fig. S11b), ΔI_p is markedly proportional to the logarithm of the PTK7 concentration (log C_{PTK7}) (inset in Fig. S11b). The equation ΔI_p (μA) = 31.52 + 9.91 log C_{PTK7} (ng mL^{-1}) with R^2 = 0.985 and an LOD of 0.66 pg mL^{-1} at an S/N ratio of 3 were obtained. Compared with previously reported PTK7 aptasensors (Table 1), the proposed sensor exhibits lower detection limits and a broader PTK7 linear range, thereby suggesting its superior sensing performance.

3.6. Selectivity, reproducibility, and stability of the proposed aptasensor

The selectivity of the Zn-MOF-on-Zr-MOF-based electrochemical aptasensor was measured by examining its response to the interferences, including lysozyme, mouse immunoglobulin G, prostate-specific antigen, vascular endothelial growth factor, human epidermal growth factor receptor-2, and their mixed solution, all of which can coexist with PTK7 in human serum. The concentration of the interferences (0.1 ng mL^{-1}) is 100-fold that of PTK7 (0.001 ng mL^{-1}). The results of the selectivity assessment of PTK7 by EIS are summarized in Fig. 4e; here, the ΔR_{ct} caused by the addition of interferences are supplied. Whereas significant changes in ΔR_{ct} were observed during detection of PTK7 and the mixed solution containing PTK7, negligible response variations were obtained with addition of other interferences. The results reveal the high selectivity of the developed aptasensor for PTK7 due to the highly specific recognition between PTK7 and its corresponding aptamer probe.

The reproducibility and stability of the sensor were investigated to verify its potential application in clinical diagnosis and biological monitoring. The reproducibility of the aptasensor was tested by detecting the ΔR_{ct} caused by addition of PTK7 (0.001 ng mL^{-1}) at room temperature (25 °C) with five Zn-MOF-on-Zr-MOF-based aptasensors prepared under the same conditions (Fig. 4f). The observed relative standard deviation (RSD) for ΔR_{ct} of the five aptasensors for detecting PTK7 was very small at only 2.54%. During storage of the Zn-MOF-on-Zr-MOF-based aptasensor in a refrigerator at 4 °C for 15 d, EIS measurements were carried out in 0.1 M PBS containing 0.001 and 1 ng mL^{-1} PTK7 every day. The obtained ΔR_{ct} values are illustrated in Fig. S12. No apparent change in response to 0.001 and 1 ng mL^{-1} PTK7 was observed, and very low RSDs of 3.38% and 1.24%, respectively, were obtained. These results reveal that the proposed aptasensor not only exhibits low detection limits and high selectivity but also possesses good stability and reproducibility. Integration of various Zn-MOF and Zr-MOF materials can enhance the binding interaction between the formed G-quadruplex structure and the MOF substrate, leading to high sensitivity, good stability, and reproducibility. Compared with single metallic MOFs-based aptasensors, the sensing performance of bimetallic MOF-based sensors can be freely modulated for different analytes.

3.7. Real sample analysis

To verify the applicability of the proposed sensing platform, we investigated its practical use in real samples by detecting PTK7 in human serum samples. Different PTK7 concentrations were spiked into treated human serum samples, and the presence of PTK7 was detected and analyzed using the Zn-MOF-on-Zr-MOF-based aptasensor through EIS. The standard curve is shown in Fig. 4d, and the obtained concentrations of PTK7 were simulated and illustrated in Table S5. The recovery of the proposed aptasensor ranged from 96.6% to 104.6%, with RSDs less than 5%. Thus, this new strategy exhibits excellent sensing performance, including high sensitivity, excellent selectivity, good stability, reproducibility, and acceptable feasibility for rapidly detecting PTK7 in human serum.

4. Conclusions

In summary, we synthesized two bimetallic ZnZr-MOFs, including Zn-MOF-on-Zr-MOF and Zr-MOF-on-Zn-MOF, and exploited them as scaffold substrates for immobilizing aptamer strands and sensing the cancer marker PTK7. Owing to the relatively large pore size of Zr-MOF, penetration of Zn(II) ions into the interior of Zr-MOF and formation of a layer-on-layered bimetallic MOF are feasible. The Zn-MOF nanosheets are bonded to the Zr-MOF layer, unlike the free nature of the layer-on-layer structured Zr-MOF-on-Zn-MOF hybrid. Compared with the Zr-MOF- and Zr-MOF-on-Zn-MOF-based aptasensors, the Zn-MOF- and Zn-MOF-on-Zr-MOF-based aptasensors exhibited higher binding interactions with the G-quadruplex of aptamer strands and PTK7 since the free adsorption of aptamer strands allows their easy binding with PTK7. The proposed Zn-MOF-on-Zr-MOF-based aptasensor showed excellent biosensing capacity, stability, reproducibility, and applicability. Considering the great diversity and tunability of MOF-on-MOF materials, the present work provides a new method for fabricating bimetallic MOF-based aptasensors for specific targeting of cancer markers. The

Table 1
Comparisons of the proposed approach with other electrochemical techniques for the detection of PTK7.

Materials	Detection method	Detection range	LOD	Ref
DNA-AgNCs	fluorescence	3.84 − 256 ng mL^{-1}	1.6 ng mL^{-1}	(Z. Liu et al. 2017)
DNA-AuNPs/aptamer/AuNPs/Nf	DPV	0.13 − 13 ng mL^{-1}	0.048 ng mL^{-1}	(Miao et al., 2016)
$[Ir(pbi)_2(5,5\text{-dmbpy})]PF_6$	luminescence	0 − 4.8 μg mL^{-1}	13 ng mL^{-1}	(Lin et al., 2015)
Structure-switching aptamer	fluorescence	0.63 − 1000 ng mL^{-1}	0.13 ng mL^{-1}	(Wang et al., 2015)
ZnO nanodisks @g-C_3N_4	Time-based photocurrent responses	20 − 2 × 10^4 cell mL^{-1}	20 cell mL^{-1}	(Pang et al., 2018)
FAM-labelled DNA strands	fluorescence	50 − 1 × 10^6 cell mL^{-1}	15 cell mL^{-1}	(Fan et al., 2016)
Zn-MOF-on-Zr- MOF	EIS	0.001 − 1 ng mL^{-1}	0.84 pg mL^{-1}	**This work**
	DPV	0.001 − 1 ng mL^{-1}	0.66 pg mL^{-1}	

fabrication of new MOF-based biosensors is essential for timely clinical diagnosis and treatment of diseases.

Acknowledgment

This work was supported by Programs for the National Natural Science Foundation of China (NSFC: Account Nos. 81601082, 81371363, U1604127 and U1704256), and Innovative Technology Team of Henan Province Technology of China (CXTD2014042).

Appendix A. Supporting information

Supplementary data associated with this article can be found in the online version at doi:10.1016/j.bios.2018.09.079.

References

Asha, K.S., Bhattacharjee, R., Mandal, S., 2016. Angew. Chem. Int. Ed. 55, 11528–11532.
Bellarosa, L., Brozek, C.K., García-Melchor, M., Dincă, M., López, N., 2015. Chem. Mater. 27, 3422–3429.
Chen, R., Yao, J., Gu, Q., Smeets, S., Baerlocher, C., Gu, H., Zhu, D., Morris, W., Yaghi, O.M., Wang, H., 2013. Chem. Commun. 49, 9500–9502.
Chen, Y., Munteanu, A.C., Huang, Y.F., Phillips, J., Zhu, Z., Mavros, M., Tan, W., 2009. Chem. -Eur. J. 15, 5327–5336.
Chuah, G.K., Jaenicke, S., Cheong, S.A., Chan, K.S., 1996. Appl. Catal. A-Gen. 145, 267–284.
Cumpson, P., 2000. Surf. Interface Anal. 29, 403–406.
Dash, J., Waller, Z.A.E., Pantoş, G.D., Balasubramanian, S., 2011. Chem. -Eur. J. 17, 4571–4581.
Fan, D., Wu, C., Wang, K., Gu, X., Liu, Y., Wang, E., 2016. Chem. Commun. 52, 406–409.
Fang, G., Zhou, J., Cai, Y., Liu, S., Tan, X., Pan, A., Liang, S., 2017. J. Mater. Chem. A 5, 13983–13993.
Gao, Z.F., Chen, D.M., Lei, J.L., Luo, H.Q., Li, N.B., 2015. Anal. Chim. Acta 897, 10–16.
Gu, Y., Wu, Y.N., Li, L., Chen, W., Li, F., Kitagawa, S., 2017. Angew. Chem. Int. Ed. 56, 15658–15662.
Guo, C., Su, F., Song, Y., Hu, B., Wang, M., He, L., Peng, D., Zhang, Z., 2017. ACS Appl. Mater. Inter. 9, 41188–41199.
He, L., Duan, F., Song, Y., Guo, C., Zhao, H., Tian, J., Zhang, Z., Liu, C., Zhang, X., Wang, P., Du, M., Fang, S., 2017. 2D Mater. 4, 25098.
He, L., Zhang, Y., Liu, S., Fang, S., Zhang, Z., 2014. Microchim. Acta 181, 1981–1989.
Hou, W., Liu, Y., Zhang, B., He, X., Li, H., 2017. Adv. Mater. Interfaces 4, 1700958.
Huang, X., Liu, Y., Yung, B., Xiong, Y., Chen, X., 2017. ACS Nano 11, 5238–5292.
Jia, X., Dong, S., Wang, E., 2016. Biosens. Bioelectron. 76, 80–90.
Jung, P., Sommer, C., Barriga, F.M., Buczacki, S.J., Hernando-Momblona, X., Sevillano, M., Duran-Frigola, M., Aloy, P., Selbach, M., Winton, D.J., Batlle, E., 2015. Stem Cell Rep. 5, 979–987.
Jung, S., Kim, Y., Kim, S., Kwon, T., Huh, S., Park, S., 2011. Chem. Commun. 47, 2904–2906.
Lin, S., Gao, W., Tian, Z., Yang, C., Lu, L., Mergny, J., Leung, C., Ma, D., 2015. Chem. Sci. 6, 4284–4290.
Liu, C., Zhang, Z., Chen, M., Zhao, H., Duan, F., Chen, D., Wang, M., Zhang, S., Du, M., 2017. Chem. Commun. 53, 3941–3944.
Liu, Z., Chen, W., Han, Y., Ouyang, J., Chen, M., Hu, S., Deng, L., Liu, Y., 2017. Talanta 175, 470–476.
Ma, H., Liu, J., Ali, M.M., Mahmood, M.A.I., Labanieh, L., Lu, M., Iqbal, S.M., Zhang, Q., Zhao, W., Wan, Y., 2015. Chem. Soc. Rev. 44, 1240–1256.
Miao, X., Li, Z., Zhu, A., Feng, Z., Tian, J., Peng, X., 2016. Biosens. Bioelectron. 83, 39–44.
Narayanan, J., Sharma, M.K., Ponmariappan, S., Sarita, Shaik, M., Upadhyay, S., 2015. Biosens. Bioelectron. 69, 249–256.
Pang, X., Cui, C., Su, M., Wang, Y., Wei, Q., Tan, W., 2018. Nano Energy 46, 101–109.
Qian, J., Li, Q., Liang, L., Yang, Y., Cao, Z., Yu, P., Huang, S., Hong, M., 2016. Chem. Commun. 52, 9032–9035.
Qian, J., Li, T., Hu, Y., Huang, S., 2017. Chem. Commun. 53, 13027–13030.
Quah, H.S., Ng, L.T., Donnadieu, B., Tan, G.K., Vittal, J.J., 2016. Inorg. Chem. 55, 10851–10854.
Ren, J., Ledwaba, M., Musyoka, N.M., Langmi, H.W., Mathe, M., Liao, S., Pang, W., 2017. Coord. Chem. Rev. 349, 169–197.
Salamon, J., Sathishkumar, Y., Ramachandran, K., Lee, Y.S., Yoo, D.J., Kim, A.R., Gnana Kumar, G., 2015. Biosens. Bioelectron. 64, 269–276.
Schmitt, K., Schirmer, B., Hoffmann, C., Brandenburg, A., Meyrueis, P., 2007. Biosens. Bioelectron. 22, 2591–2597.
Shangguan, D., Cao, Z., Meng, L., Mallikaratchy, P., Sefah, K., Wang, H., Li, Y., Tan, W., 2008. J. Proteome Res. 7, 2133–2139.
Shen, W., Zhuo, Y., Chai, Y., Yuan, R., 2015. Anal. Chem. 87, 11345–11352.
Song, X., Oh, M., Lah, M.S., 2013. Inorg. Chem. 52, 10869–10876.
Sun, B., Zhao, H., Xie, B., Bai, L., Jiang, Z., Chen, J., 2017. J. Inorg. Biochem. 176, 17–23.
Tan, B., Zhao, H., Wu, W., Liu, X., Zhang, Y., Quan, X., 2017. Nanoscale 9, 18699–18710.
Tertiş, M., Florea, A., Feier, B., Marian, I.O., Silaghi-Dumitrescu, L., Cristea, A., Săndulescu, R., Cristea, C., 2015. J. Nanosci. Nanotechno. 15, 3385.
Wang, F., Yang, J., Wu, K., 2009. Anal. Chim. Acta 638, 23–28.
Wang, G., Song, C., Kong, D., Ruan, W., Chang, Z., Li, Y., 2014. J. Mater. Chem. A 2, 2213–2220.
Wang, Q., Vasilescu, A., Wang, Q., Coffinier, Y., Li, M., Boukherroub, R., Szunerits, S., 2017a. ACS Appl. Mater. Inter. 9, 12823–12831.
Wang, S., McGuirk, C.M., Ross, M.B., Wang, S., Chen, P., Xing, H., Liu, Y., Mirkin, C.A., 2017b. J. Am. Chem. Soc. 139, 9827–9830.
Wang, Y., Wu, Z., Liu, S., Chu, X., 2015. Anal. Chem. 87, 6470–6474.
Wu, Y., Zou, L., Lei, S., Yu, Q., Ye, B., 2017. Biosens. Bioelectron. 97, 317–324.
Xie, B., Qiu, G., Hu, P., Liang, Z., Liang, Y., Sun, B., Bai, L., Jiang, Z., Chen, J., 2018. Sens. Actuat. B-Chem. 254, 1133–1140.
Yıldız, R., 2015. Corros. Sci. 90, 544–553.
Yu, Q., Wu, Y., Liu, Z., Lei, S., Li, G., Ye, B., 2018. Biosens. Bioelectron. 107, 178–183.
Zhang, H., Ma, Y., Xie, Y., An, Y., Huang, Y., Zhu, Z., Yang, C.J., 2015. Sci. Rep. -UK 5, 10099.
Zhang, Z., Duan, F., Tian, J., He, J., Yang, L., Zhao, H., Zhang, S., Liu, C., He, L., Chen, M., Chen, D., Du, M., 2017. ACS Sens. 2, 982–989.
Zhao, J., Wang, Y., Dong, W., Wu, Y., Li, D., Zhang, Q., 2016. Inorg. Chem. 55, 3265–3271.
Zhao, M., Deng, C., Zhang, X., 2014. Chem. Commun. 50, 6228–6231.
Zhou, X., Tang, Y., Xing, D., 2011. Anal. Chem. 83, 2906–2912.
Zhu, Q., Xu, Q., 2014. Chem. Soc. Rev. 43, 5468–5512.